Late Carboniferous-Early Permian geodynamic evolution of NW Iran: Zircon U-Pb ages, Hf isotopes, and whole rock geochemistry of Salmas amphibolites

Robab Hajialioghli, Mohssen Moazzen, Sorraya Saeidi, Ali Mohammadi, Oscar Laurent

Late Carboniferous-Early Permian geodynamic evolution of NW Iran: Zircon U-Pb ages, Hf isotopes, and whole rock geochemistry of Salmas amphibolites

Robab Hajialioghli[a*], Mohssen Moazzen[a,b], Sorraya Saeidi[a], Ali Mohammadi[c], Oscar Laurent[d,e]

a *Department of Earth Sciences, University of Tabriz, 51666, Tabriz, Iran*
b *Department of Earth and Environmental Sciences, University of Central Asia, 736000, Khorog, Tajikistan*
c *Eurasia Institute of Earth Sciences, Istanbul Technical University, Maslak, 34467 Sarıyer/İstanbul, Turkey*
d *Department of Earth Sciences, Institute of Geochemistry and Petrology, ETH Zentrum, Clausiusstrasse 25, 8092 Zürich, Switzerland*
e *CNRS, Observatoire Midi-Pyrénées, Géosciences Environnement Toulouse UMR5563-CNRS-UPS-IRD-CNES, 14 avenue Edouard Belin, F-31400 Toulouse, France*

*Corresponding Author: hajialioghli@tabrizu.ac.ir

ABSTRACT

We report new geochronological, petrological and geochemical data from the amphibolites of the Salmas metamorphic complex of NW Iran, where Sanandaj-Sirjan magmatic-metamorphic, Urmia-Dokhtar magmatic and the Eastern Anatolian Plateau meet with a complex geodynamic history. The amphibolites are alternating with gneiss and crystallized limestone layers, and as enclaves with different sizes in gneiss. Fine- to medium-grained amphibole, plagioclase ± clinopyroxene, exhibiting a granoblastic texture, are the dominant minerals. Amphibolites are covered by Permian to Jurassic sedimentary rocks and occasionally Miocene sediments with angular discontinuity. On the basis of whole rock geochemistry, the investigated amphibolites have relatively high TiO_2 (1.23 to 2.62 mass%) and low MnO (0.18 to 0.21 mass%) contents which classify them as ortho-amphibolite. The parental magma was sub-alkaline basaltic with tholeiitic affinities, which occurred in a within-plate tectonic setting, characterized by enrichment in LREE relative to HREE and lack of Nb, Ta, Ti anomalies together with Eu negative and Ba positive anomalies. $\varepsilon Hf_{(t)}$ and $^{176}Hf/^{177}Hf$ of dated zircons indicate a depleted mantle to lower

crust origin for the parental magma of the amphibolites. U-Pb dating on zircon grains gives mean ages of 304.8 Ma, corresponding to magmatism during Late Carboniferous-Early Permian as the signature of magmatism related to the opening of the Neotethys Ocean. Thermal effect of the Late Cretaceous to Early Cenozoic subduction-related magmatic events have been recorded by zircon grains of the investigated amphibolites asovergrown metamorphic zircon around original magmatic grains.

Keywords: Neotethys, amphibolite geochemistry, Zircon U-Pb-Hf isotopes, SE Salmas, NW Iran

1. Introduction

Opening, spreading, subduction and closure of the Neotethys ocean played a major role in the geodynamic evolution of the Alpine-Himalayan Orogenic belt. Subducting of the Paleotethys oceanic crust followed by the opening of the Neotethys ocean along the northern margin of Gondwana (Stampfli et al., 2013). Opening of the Neotethys is marked by several occurrences of Late Palaeozoic ferroan (A-type) and alkaline felsic plutonic and volcanic magmatism in Iran and adjacent areas (Fig. 1). Late Palaeozoic intrusive rocks related to opening of Neotethys occur mainly in the Sanandaj-Sirjan Zone and NW Iran with zircon U-Pb ages of Late Carboniferous-Early Permian (Fig. 1 and Table 1). A-type volcanic rocks at the opening stage of Neotethys are scarce (Delavari et al., 2019). Nabatian et al., (2021) consider A-type rhyolites from NW Iran as Neothetys-related magmatism. In addition, detrital zircons with Carboniferous ages were recorded from Late Cretaceous turbiditic sandstones in NW Iran (Mohammadi et al., 2022). There is not much published work on mafic rock magmatism associated with opening of Neotethys. Late Paleozoic alkaline and sub-alkaline amphibolites and gabbros from Doroud and Azna areas, are considered by Shakerardakani et al., (2015) as a result of Neotethys opening. Neotethys rift-related rocks in Oman are considered to be Permian, on the basis of

Palaeomagnetic data (e.g. Besse et al., 1998) and pelagic sediments associated with basaltic volcanism (Searle and Graham, 1982; Blendinger et al.,1990; Pillevuit et al., 1997).The westward Neotethys propagation from Oman to northwestern Arabia during Permian is proposed by Frizon de Lamotte et al., (2013). The opening stage of Neothetys in NW Iran is not attended adequately. Studies on mafic magmatism is particularly scarce in this regrad amphibolites from NW Iran, as mafic magmatism can help to study geomechanism and timing of opening stage of Neotethys, which in turn can help to get a broader idea of geodynamic evolution of NW Iran, Eastern Anatolia and Lesser Caucasus during Late Carboniferous-Early Permian. For this we provide here new findings on geological, petrological and mineralogical characteristics of amphibolites from the Salmas area in NW Iran. Using whole rock, U-Pb zircon ages and Hf isotope compositions, we will show that parental magma of these amphibolites formed in a within plate tectonic extensional setting at the opening stage of Neotethys.

2. Geological background and field relations

The SE Salmas metamorphic complex is located at the west of Urmia Lake (NW Iran) at the junction of Central Iran and Sanandaj-Sirjan geological zones, within the Alpine-Himalayan orogenic belt (Fig 1). The Salmas area shares several geological and structural features with the Sanandaj-Sirjan zone (e.g. Khodabandeh and Aminifazl, 1993a-b; Mehdipour Ghazi and Moazzen, 2015). The Sanandaj-Sirjan zone with NW-SE trend is a belt of metamorphic (mainly greenschist to amphibolite facies) and plutonic rocks (Mohajjel and Fergusson, 2000). Continuation of this zone to NW Iran makes a complex geological setting at the vicinity of east Turkey and Lesser Caucasus with Late Neoproterozoic-Early Cambrian basement metamorphic rocks (Hassanzadeh et al., 2008). The Cadomian crustal fragments are welded to the Palaeozoic-Mesozoic terranes, and in turn are covered by vast Cenozoic volcanic rocks (Shafaii Moghadam

et al., 2015. A-type magmatism with alkaline to tholeiitic affinities is taken to represent a rapid block uprising in NW Iran due to upwelling of asthenospheric plume during Late Palaeozoic (Late Carboniferous-Early Permian). Extensional basins brought about by block uprising, is characterized by a thick sequence of Permian-Triassic sediments (Azizi et al., 2017).

Field studies in the Salmas area show that the SE Salmas metamorphic complex is similar to the Sanandaj-Sirjan in terms of rock types and structures. The oldest rock units in the area are a set of metamorphic rocks, including a metamorphic sequence of volcano-sedimentary rocks and meta-granites to meta-diorites (Fig. 2). Neoproterozoic Kahar formation (Etemad-Saeed et al., 2016), a weakly metamorphosed sedimentary unit, covers the basment metamorphic rocks with a tectonic contact. The SE Salmas metamorphic complex is consisted of amphibolite, greenschist, meta-rhyolite, marble and feldspathic gneiss (Fig. 3a -b). Amphibolites have sharp contact with gneiss and can be found as enclaves in gneiss (Fig. 3c). They appear as fine- to medium-grained rocks indicating more likely a basaltic and diabasic protolith (Fig. 3d). The Permian rocks (Ruteh and Doroud formations, Fig. 2) are characterized by sandstone at the bottom and limestone at the top, similar to Doroud and Ruteh formations of Zagros orogen. The Permian rocks placed over the metamorphic complex with a fault contact and have been intruded by the Late Cretaceous intrusives (Khodabandeh and Aminifazl, 1993a-b; Lechmann et al., 2018). Triassic and Jurassic rocks are made from thin layers of marl, dolomite, and alternation of shale and sandstone (Fig. 2). Towards the top, sediments contain microfossils indicating Lias age which are covered by Miocene sediments with angular discontinuity (Khodabandeh and Aminifazl, 1993a-b). Late Paleozoic mafic and felsic intrusive rocks make considerable outcrop exposures in the area (Fig. 2). Qushchi granite is the largest batholith in the area intruded into the Precambrian and Palaeozoic units. Melano-gabbros to diorites are mafic to intermediate rocks which are Late Paleozoic in age (Shafaii Moghadam et al., 2015).

3. Samples and analytical method

Twenty samples of amphibolite were chosen for petrography and textural relations studies. Five representative samples with fewer alteration effects were chosen for whole rock geochemical analyses (Table 2). Two samples (SS20B and SS20F) were selected for zircon U-Pb age dating (Supplumentary Table 1), and *in-situ* zircon Hf isotopic analysis (Table 3).

Whole rock analyses were carried out using XRF and ICP-MS method for major oxides and trace and rare earth elements in the MS Analytical Company in Canada. About 1kg of each sample was crashed using a steel jaw crusher and then was pulverized to 200 mash or 75 microns. To analyze the samples for major, minor and trace elements, known amount of sample was mixed with lithium metaborate and were fused on gas heater. The resulted beads were used for XRF analysis of major oxides. They used for ICP-MS analyses after four acid "near total" digestion. International standards were used for calibrations. The uncertainties for major oxides is better than ±2% and for the minor and trace elements is less than 5%.

For *in-situ* zircon U-Pb dating and Hf isotope analyses, rock samples were initially crushed using a jaw crusher to obtain smaller fragments. These fragments were then further grounded to a fine powder using a disc mill, achieving a particle size of less than 500 microns. The grounded material was sieved, retaining the fraction between 60 and 250 microns. Standard heavy-liquid and magnetic separation methods delivered heavy mineral fractions enriched in zircons. Zircons of grain fraction 60–250 μm were handpicked under a binocular microscope (fine-, medium- and coarse- grained). Different size of selected grains were mounted in three epoxy blocks using U- and Pb-free resin, polished to expose the internal parts of the grains, and coated with carbon.

Suitable zircon domains identified with cathodoluminescence (CL) and back-scattered images obtained by split screen on a CamScan CS44 Scandunk Viermalning electron microscope

(SEM; Tescan a.s., Brno) at ETH-Zurich. Zircon characteristics were interpreted following Corfu et al., (2003). The zircons were analyzed for U-Pb isotopes by Laser Ablation Inductively Coupled Mass Spectrometry (LA-ICP-MS) at at the Institute of Geochemistry and Petrology, ETH Zurich using an Excimer (ArF 193 nm) RESOlution (Australian Scientific Instruments/Applied Spectra) laser ablation system equipped with a dual-volume S-155 ablation cell (Laurin Technic, Australia), coupled to an Element XR (Thermo Scientific, Germany) sector-field ICP-MS. We used a laser repetition rate of 5 Hz, energy density of ca. 2.5 J/cm^2 and spot diameter of 29 μm. Carrier gas consisted of high-purity He (ca. 0.5 L/min) to which was admixed high-purity Ar sample gas from the ICP-MS (ca. 1.0 L/min) directly in the ablation funnel. The signal was homogenized downstream of the ablation cell using an in-house Squid tubing. Data acquisition time per spot was about 1 min (30 s gas blank + 30 s ablation). The list of analyzed isotopes and further details about the methods are provided in Supplumentary Table 1.

The data were processed with the Igor Pro Iolite v2.5 software (Hellstrom et al., 2008), using the VizualAge data reduction scheme (Petrus and Kamber, 2012). Laser-induced element fractionation (corrected after Paton et al., 2010), instrumental mass discrimination and drift through the analytical session were corrected by standard bracketing against zircon reference material GJ-1 (using isotope ratios recommended by Horstwood et al., 2016). The quoted uncertainties for each individual analysis correspond to the internal error and propagated uncertainty based on the scatter of the primary reference material (see Paton et al., 2010). The accuracy and reproducibility within each run of analysis were monitored by periodic measurements of zircon reference materials Plešovice (337 Ma; Sláma et al., 2008) and 91500 (1065 Ma; Wiedenbeck et al., 1995). The U-Pb dates obtaied from both zircon reference materials are within uncertainty identical to the reference values (see Supplumentary Table 1). Concordia diagrams were made using ISOPLOT v.3.0 (Ludwig, 2003).

Analyses of Lu-Hf isotopic compositions were performed on the same zircon grains which were used for U-Pb dating, by positioning the spots "on top" of the existing U-Pb laser spots or within the same growth zones. The analyses were performed at ETH Zurich, using the same laser model as for U-Pb geochronology, but attached to a Nu Plasma 2 MC-ICP-MS (Nu Instruments Ltd., UK). We have used a laser repetition rate of 5 Hz, energy density of ca. 4 J/cm^2 and spot diameter of 40 µm. Carrier gas consisted in high-purity He (ca. 0.38 L/min) to which was admixed high-purity Ar sample gas from the ICP-MS (ca. 0.9 L/min) in the ablation funnel. A typical run consisted in a 40 s background measurement followed by 40 s zircon ablation. The data were processed with the Igor Pro Iolite v2.5 software (Hellstrom et al., 2008), using an in-house data reduction scheme. The βHf and βYb mass bias coefficients were calculated using an exponential law from measured $^{179}Hf/^{177}Hf$ and $^{173}Yb/^{171}Yb$ respectively, and using natural abundance ratios ($^{179}Hf/^{177}Hf = 0.7325$ and $^{173}Yb/^{171}Yb = 1.132685$) from Chu et al. (2002). The isobaric interferences of ^{176}Yb and ^{176}Lu on ^{176}Hf were subsequently corrected using the natural abundance ratios ($^{173}Yb/^{176}Yb = 0.79618$ and $^{175}Lu/^{176}Lu = 0.026549$) from Chu et al., (2002). The Lu mass bias correction factor was assumed to be the same as that of Yb. The accuracy and precision of the results obtained were monitored through the systematic measurements of the well-characterized Temora-2 (Woodhead and Hergt, 2005), Mud Tank (Woodhead and Hergt, 2005), and Plešovice (Sláma et al., 2008) zircon reference materials. The standard reference materials were chosen as to show a range in Yb/Hf ratios to test the accuracy of the ^{176}Yb correction following the recommendations of Fisher et al., (2014). Repeated analyses of standards yielded the following $^{176}Hf/^{177}Hf$ ratios for the analytical session: Temora-2 = 0.282683 ± 25 (2 SD; n = 37); Plešovice = 0.282474 ± 31 (2 SD; n = 17); Mud Tank = 0.282494 ± 38 (2 SD; n = 21), which are all within uncertainties overlapping the published reference values (Fisher et al., 2014). Age corrections to calculate initial $^{176}Hf/^{177}Hf$ ratios and εHf values were obtained using a

^{176}Lu decay constant of 1.867×10^{-11} year^{-1} (Scherer et al., 2001) and the chondritic uniform reservoir (CHUR) parameters of Bouvier et al., 2008).

4. Petrography of amphibolites

Amphibolites of the study area are epidote amphibolite, plagioclase-hornblende amphibolite, biotite amphibolite and clinopyroxene-biotite amphibolite. Epidote amphibolites are exposed mainly around the Ghalghanchi village (Fig. 2) and are composed of amphibole (60-65 Vol%), plagioclase (20-25 Vol%), epidote (5-10 Vol%) and rare amounts of quartz and Fe-Ti oxides. The main texture is granoblastic with weak orientation. Epidote appears as metamorphic mineral phase in textural equilibrium with other minerals. Epidote-biotite amphibolites are fine-to medium- grained rocks exposed around west of Urmia Lake (Fig. 2) and are formed from amphibole (35-40Vol%), plagioclase (25-30 Vol%), biotite (10-15 Vol%) and epidote (5-10 Vol%). Rare quartz and Fe-Ti oxides are minor phases in these rocks. The rocks are oriented. Plagioclase-hornblende amphibolites crop out mainly around the Aghziarat village (Fig. 2). They are dark green in hand specimens and are made of amphibole (50-55 Vol%) and plagioclase (30-35 Vol%). Other mineral phases include Fe-Ti oxides, ilmenite (~5 Vol%), and rare quartz, titanite and zircon (all ~ 5 Vol%). Fine-grained rocks show slight preferred orientation brought about by plagioclase and amphibole lineation, while medium-grained rocks show mosaic textures. Fe-Ti oxides are changed to titanite at the mineral margins. Samples from this type of amphibolite are the most fresh rocks with minimum alteration effects. Biotite amphibolites also can be found around Aghziarat and Ghalghanchi villages (Fig. 2). These rocks are pale green in hand samples and show relatively high alteration effects. The rocks consist of amphibole (50-55 Vol%), plagioclase (25-30 Vol%), biotite (5-10 Vol%) along with minor phases such as quartz, titanite and Fe-Ti oxides. The main texture in these types of samples is porphyro-granoblastic

with relatively larger amphibole porphyroblasts in a fine-grained groundmass made of plagioclase. Plagioclase shows alteration to clay minerals. Clinopyroxene-biotite amphibolites crop out around Gharabagh village (Fig. 2), containing amphibole (55-60 Vol%), plagioclase (15-20 Vol%), biotite (10-15 Vol%) and clinopyroxene (5-10 Vol%), along with subordinate amounts of quartz and opaque minerals

5. Discussion

5.1. Whole rock chemistry and tectonomagmatic evolution

The high proportion of amphibole (hornblende) and plagioclase, rare quartz, and lack of carbonate minerals in the studied amphibolites indicate an igneous protolith for them. To confirm this, whole rock geochemical data are used. MnO, TiO_2, Cr and Ni contents of the analyzed samples using criteria of Leake, (1964) and Misra (1971) show an igneous protolith, and the rocks are ortho-amphibolite. Relatively immobile elements during alteration and amphibolite facies metamorphism such as Ti, Zr, Ga and Ce are used to determine magmatic composition of amphibolite protolith. In the SiO_2 *vs* Zr/TiO_2 diagram of Floyd and Winchester, (1978) the samples show basaltic composition of protolith magma (Fig. 4a). Using classification diagram of Le Bas et al., (1986) verify the result above. The magma was sub-alkaline with tholeiitic nature (Fig. 4b). Basalts tectonic setting discrimination diagrams (Pearce and Cann, 1973; Schandl and Gorton, 2002) reveal a within plate tectonic setting for the studied rocks (Fig.4 c-d). Based on the TiO_2- K_2O- P_2O_5 contents, the studied samples show within plate basalts affinities (Pearce et al., 1975).The basaltic protolith originated from an enriched mantle source (Fig. 5). Gabbro-norite samples from Qushchi (Fig. 2) studied by Shafaii Moghadam et al., (2015) share similar geochemical and tectonomagmatic characteristics with amphibolite samples studied here. Chondrite-normalized REE patterns for all amphibolite samples are parallel with relative

enrichment of LREE compared to HREE, without distinct negative Eu anomaly (Fig.6a). LREE enrichment, specially La, can be attributed to crystal fractionation and depletion in HREE such as Yb and Lu, which may indicate presence of garnet in the source materials as a residual phase. Trace elements patterns normalized to EMORB, are similar to those of within plate basalts (Fig.6b). Lack of negative anomaly for Ti, Nb and Ta along with high Nb and Ta contents compared to primary mantle, all support a within plate origin for the protolith basaltic magma (e.g. Edwards et al., 1994; Zou et al., 2000). Relatively high Th and U contents (Fig. 6b) and positive Ba anomaly (Pearce and Stern, 2006) support contribution of continental crust materials.

5.2. Hf ISOTOPES

Hf isotopic composition of zircon can help to find out the origin of magmatic rocks, especially those which are evolved in later processes including metamorphism and were subject to lead loss (Griffin et al., 2000) since Hf isotopic ratios remains unchanged. The Lu/Hf ratios in zircon are low, this is the main reason that present-day and initial Hf isotope ratios are almost identical. Hf isotopic ratios in continental crust inherit from original mantle materials. Crustal Hf isotopic composition can be non-radiogenic ($\varepsilon Hf<0$) or radiogenic ($\varepsilon Hf>0$). The crustal materials show origin from an enriched mantle in the first case and a depleted mantle in the second (Griffin et al., 2000). Hf isotopic composition for a magma formed from a young crust generated from a depleted mantle., will be similar to the mantle compositions. Hf isotopic composition for magma formed from an old crust will be non-radiogenic (Griffin et al., 2000). Negative epsilon Hf values are produced mainly by the reworking (remelting) of existing crust, while positive values are indicative of a mantle source. Reworking of juvenile crustal reservoirs with short crustal residence times can yield also positive epsilon Hf values. Hf isotopic data and variation of εHf for the analyzed zircons from the SE Salmas amphibolites, along with uncertainties are presented in Supplementary Table 1. 12 spots in sample SS20B and 10 spots in sample SS20F zircons are

analyzed for Hf isotopes. $^{176}Hf/^{177}Hf$ in magmatic parts of zircons with zoning in sample SS20B varies from 0.282831 to 0.282996 and εHf is 8.4 to 14.3. $^{176}Hf/^{177}Hf$ in overgrown metamorphic zircons at the outer rims ranges from 0.282837 to 0.283029 and εHf is 7.5 to 13.7 (Table 3). All $^{176}Hf/^{177}Hf$ ratios analyzed in zircons from sample SS20F are from magmatic grains which are in the range of 0.282773 to 0.282790 and εHf is 6.3 to 8.2. Only one zircon grain has lower $^{176}Hf/^{177}Hf$ of 0.282630 and εHf of 0.9 which can show crustal materials contribution in magma (Table 3). According to Corfu and Stott, (1993), εHf values of 1.7 show crustal materials in magma generation as extensive contamination or direct partial melting of the lower crust. εHf values of 1.4 are related to crustal assimilation at lower crustal levels. Considering the lower age for this zircon grain (276 Ma), compared to other ages (294.9 to 313.5 Ma), more likely it represents direct melting of the lower crust. Fig.7a,b show U-Pb ages against $^{176}Hf/^{177}Hf$ and εHf (from Vertoort et al., 1999; Hawkesworth et al., 2010; Dhuime et al., 2011) for the analyzed grains. All magmatic zircons (with εHf of 6.3 to 8.2 for sample SS20F and εHf of 8.4 to 14.3 for sample SS20B) in both samples plot between Chondrite uniform reservoir (CHUR) and depleted mantle (DM), which clearly show that the protolith magma was formed from a depleted mantle source with some crustal magma contribution (Fig.7a-b). Data from metamorphic overgrown zircons with ages of 99.8 to 108.5 Ma and one zircon 65.4 Ma old (from sample SS20B) with high εHf, for which $^{176}Hf/^{177}Hf$ are relatively higher. O'Reilly et al., (2008) consider high $^{176}Hf/^{177}Hf$ ratios in new metamorphic zircons relative to older magmatic zircons as a result of lower Lu/Hf in magmatic zircons in protolith or due to effect of metamorphic fluids. Following crystallization of igneous zircon, Hf mainly inters zircon structures, while Lu enters other silicate phases. Therefore, new zircons crystallizing in late magmatic phases or metamorphism, contain more Lu, resulting in more radiogenic ^{176}Hf content (O'Reilly et al., 2008).

5.3. Age Data applications

113 out of 115 analyses spots from zircons in sample SS20F give concordant ages about 300 Ma and two other spots give ages of 287 and 276 Ma (Fig.8a-b). Age data from sample SS20B are more scattered (V 8c-d). 37 spots were analyzed on zircons in this sample. 10 spots give ages of 385-291 Ma, 12 spots are 108.5 to 99.1 Ma old and 5 spots have ages of 65.8 to 45.3 Ma (Fig.8c-d).

We interpret ages around 300 Ma (Late Carboniferous-Early Permian) as the zircon crystallization age from magma. Late Carboniferous-Early Permian ages for the protolith of the studied amphibolites are similar to Late Paleozoic mafic to intermediate magmatism in the Sanandaj-Sirjan and felsic magmatism in NW Iran (Fig.1 and Table 1).

Ages of 108.5 to 99.8 Ma can be attributed to thermal effects of island arc initaition of the Neotethys subduction (e.g. Lechmann et al., 2018). Much younger ages of 65.8 to 45.3 Ma (although very few) can be attributed to the continental collision stage. Shafaii Moghadam et al., (2020) interpreted similar U-Pb ages of 110-80 Ma and 75-50 Ma from the Zagros Zone of Iran in relation with different magmatic episodes of extension and compression during subduction initiation and arc magmatism of Neotethys, respectively. Geochemistry and age data of the amphibolites studied here indicate their protolith formation in an extensional (rifting) tectonic setting during Late Carboniferous-Early Permian. Many studies consider Late Palaeozoic magmatism as opening phase of Neotethys. As mentioned in the introduction section, alkaline intrusive and extrusive magmatism in Iran and the adjacent areas are taken as evidence for crustal extension followed by Neotethys opening. Considering these findings and amphibolites studied here, a tectonic model for opening of the Neotethys ocean and closure of Palaeotethys is proposed (Fig. 9). Neotethys ocean rifting occurred during Late Carboniferous-Early Permian. Island arc magmatism (e.g. Jan complex, Mohajjel et al., 2003, Fig.9) along with olistostrome

sedimentary fragments in Iran and Oman ophiolites (Knipper et al., 1986), and I-type plutonic rocks in central and NW Iran as active continental margin with an average ages of Jurassic-Cretaceous (Shahabpour, 2005; Lechmann et al., 2018) can be taken as evidence for two simultaneous subduction in the Neotethys ocean basin. Zircon ages of 108.5 to 99.8 Ma may show the subduction initiation in mid-Cretaceous (e.g. Shafaii Moghadam et al., 2020). Concerning collision time of Arabian plate with Central Iran Zone, there are some controversies from Late Cretaceous (Berberian and King, 1981) to Miocene (Berberian and Berberian, 1981) or uppermost Pliocene (Stöcklin, 1968). There is a growing body of evidence in support of Late Eocene to Oligocene initial collision (e. g. Jolivet and Faccenna, 2000; Agard et al., 2005; Vincent et al., 2005; Ballato et al., 2010, Cai et al., 2021) to final collision of Late Miocene–Early Pliocene (Ao et al., 2016). Young ages of 65.8 to 45.3 Ma from this research can be attributed to island arc magmatic thermal effects.

6. Conclusions

Amphibolites from the SE Salmas metamorphic complex are associated with greenschist, meta-rhyolite, marble and feldspathic gneiss with a continental crust affinity. Petrographic features along with chemical compositions show that they are ortho-amphibolites generated from an igneous protolith with a sub-alkaline basaltic nature and tholeiitic affinities. $\varepsilon Hf_{(t)}$ and $^{176}Hf/^{177}Hf$ of dated zircons indicate a depleted mantle to lower crust origin for the parental magma of the amphibolites. Zircon U-Pb ages show that the magma occurred in a continental within plate setting during Late Carboniferous-Early Permian as the signature of magmatism related to the opening of the Neotethys Ocean in NW Iran. Mid-Cretaceous overgrown metamorphic zircons around magmatic grains more likley show metamorphism above subduction zone. Thermal effect

of the Late Cretaceous and Early Cenozoic subduction-related magmatic is recorded by zircons in the investigated amphibolites.

Acknowlegment

This paper is a part of the Ph.D. dissertation of S. Saiedi. University of Tabriz is acknowledged for the fieldworks supports.

References

Abdulzahra, I.K, Hadi, A., Asahara, Y., Azizi, H.,Yamamoto, K., 2016. Zircon U–Pb ages and geochemistry of Devonian A-type granites in the Iraqi Zagros Suture Zone (Damamna area): New evidence for magmatic activity related to the Hercynian orogeny. Lithos, 264, 360-374.

Advay, M., Ghalamghash, J., 2011. Petrogenesis and U–Pb dating zircon of granites of Heris (NW of Shabestar), Eastern Azerbaigan province. Iranian J. Crystal. Mineral. 4, 633–648 (in Persian).

Agard, P., Omrani, J., Jolivet, L., Lepvrier, C., Kachrillo, N., 2005. Convergence history across Zagros (Iran): constraints from collisional and earlier deformation. Int. J. Earth Sci. (Geol. Rundsch.), 94, 401–19.

Alirezaei, S., Hassanzadeh, J., 2012. Geochemistry and zircon geochronology of the Permian A-type Hasanrobat granite, Sanandaj-Sirjan belt: a new record of the Gondwana break-up in Iran. Lithos, 151- 122-134.

Ao, S., Xiao, W., Khalatbari-Jafari, M., Talebian, M., Chen, L., Wan, B., … Zhan, Z., 2016. U-Pb zircon ages, field geology and geochemistry of the Kermanshah ophiolite (Iran): From continental rifting at 79 Ma to oceanic core complex at ca. 36 Ma in the southern Neo-Tethys. Gondwana Res. 31, 305-318.

Asadpour, M., Pourmoafi, S. M., Heuss, S., 2013a. Geochemistry, petrology and U-Pb geochronology of Ghazan mafic-ultramafic intrusion, NW Iran. Iranian J. Petrol. 4(14), 1-16 (in Persian).

Asadpour, M., Heuss, S., Pourmoafi, S.M. 2013b. New Evidences of Precambrian and Paleozoic Magmatism in the Gharebagh Intrusives, NW Iran. Sci. Q. J. GeoSci. 23 (89), 129-148.

Azizi, H., Kazemi, T., Asahara, Y., 2017. A-type granitoids in Hasansalaran complex, northwestern Iran: Evidence for extensional tectonic regime in northern Gondwana in the Late Paleozoic. *J. Geodyn.* 108, 56-72.

Ballato, P., Mulch, A., Landgraf, A., Strecker, M. R., Dalconi, M. C., Friedrich, A., Tabatabaei, S. H. 2010. Middle to Late Miocene Middle Eastern climate from stable oxygen and carbon isotope data, southern Alborz mountains, N Iran. Earth Planet. Sci. Lett. 300, 125- 138.

Bea, F., Mazhari, A., Montero, P., Amini, S., Ghalamghash, J., 2011. Zircon dating, Sr and Nd isotopes, and element geochemistry of the Khalifan pluton, NW Iran: Evidence for Variscan magmatism in a supposedly Cimmerian superterrane. J. Asian Earth Sci. 44, 172-179.

Berberian, F., Berberian, M., 1981. Tectono-plutonic episodes in Iran. In: Gupta, H. K., Delany, F. M. (eds.) Zagros-Hindu Kush-Himalaya Geodynamic Evolution.Geodynamics Series, 3. Am. Geophys. Union Washington DC, 5–32.

Berberian, M., King, G.C.P., 1981. Towards a paleogeography and tectonic evolution of Iran. Canadian. J. Earth Sci. 18, 210-265.

Besse, J., Torcq, F., Gallet, Y., Ricou, L. E., Krystyn, L., Saidi, A., 1998. Late Permian to Late Triassic palaeomagnetic data from Iran: Constraints on the migration of the Iranian block through the Tethyan Ocean and initial destruction of Pangaea. Geophys. J. Int. 135, 77–92.

Blendinger, W., Van Vliet, A., Hughes Clarke, M.W., 1990. Updoming, rifting and continental margin development during the Late Palaeozoic in Northern Oman. In Robertson, A. H. F., Searle, M.P., Ries, A. C. (Eds.), The Geology and Tectonics of the Oman Region. Geol. Soc. London Spec. Publ. 49, 27-37.

Bouvier, A., Vervoort, J. D., Patchett, P. J., 2008. The Lu–Hf and Sm–Nd isotopic composition of CHUR: constraints from unequilibrated chondrites and implications for the bulk composition of terrestrial planets. Earth Planet. Sci. Lett. 273, 48–57. doi:10.1016/ j.epsl.2008.06.010.

Cai, F., Ding, L., Wang, H., Laskowski, A. K., Zhang, L., Zhang, B., Mohammadi, A., Li, J., Song, P., Li, Z., Zhang, Q., 2021. Configuration and timing of collision between Arabia and Eurasia in the Zagros collision zone, Fars, southern Iran. Tectonics, 40 (8), p.e2021TC006762.

Chu, N.-C., Taylor, R. N., Chavagnac, V., Nesbitt, R. W., Boella, R. M., Milton, J. A., German, C.R., Bayon, G., Burton, K., 2002. Hf isotope ratio analysis using multicollector inductively coupled plasma mass spectrometry: An evaluation of isobaric interference corrections. *J. Anal. At. Spectrom.* 17, 1567–1574.

Corfu, F., Stott, G.M., 1993. Age and petrogenesis of two late Archean magmatic suites, northwestern Superior Province, Canada: Zircon U-Pb and Lu-Hf isotopic relations. J. Petrol. 34 (4), 817-838.

Corfu, F., Hanchar, J. M., Hoskin, P.W.O., Kinny, P., 2003. Altas of zircon textures in Zircon. Rev. Mineral. Geochem. 53 (1), 469–500).

Delavari, M., Arab Asadi, F., Mohammadi, A. 2019. Paleozoic magmatism in the southwest of Julfa (northwestern Iran): Geochemical characteristics, U-Pb dating and tectonic setting. Iranian J. Petrol. 10 (2), 99-120. (in Persian).

Dhuime, B., Hawkesworth, C., Cawood, P., 2011. When continents formed. *Sci.* 331, 154- 155.

Edwards, C.M.H., Menzies, M.A., Thirlwall, M.F., Morris, J.D., Leeman, W.P., Harmon, R.S. (1994). The transition to potassic alkaline volcanism in island arcs: the Ringgit-Beser complex, east Java, Indonesia. J. Petrol. *35, 1557–1595.*

Etemad-Saeed, N., Hosseini-Barzi, M., Adabi, M.H., Miller, N.R., Sadeghi, A., Houshmandzadeh, A., Stockli, D.F. (2016). Evidence for ca. 560 Ma Ediacaran glaciation in the Kahar Formation, Central Alborz Mountains, northern Iran. *Gondwana Res.* 31, 164-183.

Fisher, C.M., Vervoort, J.D., Hanchar, J.M. 2014. Guidelines for reporting zircon Hf isotopic data by LA-MC-ICPMS and potential pitfalls in the interpretation of these data. Chem.Geol. 363, 125–133.

Floyd, P.A., Winchester, J.A. 1978. Identification and discrimination of altered and metamorphosed volcanics using immobile elements. Chemical Geol. 21, 291-306.

Frizon de Lamotte, D., Tavakoli-Shirazi, S., Leturmy, P., Averbuch, O., Mouchot, N., Raulin, C., … Ringenbach, J.C., 2013. Evidence for Late Devonian vertical movements and extensional deformation in

northern Africa and Arabia: Integration in the geodynamics of the Devonian world. Tectonics 32, 107–122.

Griffin, W.L., Pearson, N.J., Belousova, E., Jackson, S.E., Van Achterbergh, E., O·Reilly, S.Y., Shee, S.R.. 2000. The Hf isotope composition of cratonic mantle: LAM-MC-ICPMS analysis of zircon megacrysts in kimberlites. Geoch. Cosm. Act. 64, 133-147.

Hassanzadeh, J., Stockli, D.F., Horton, B.K., Axen, G.J., Stockli, L.D., Grove, M., … Walker, J.D. 2008. U-Pb zircon geochronology of late Neoproterozoic–Early Cambrian granitoids in Iran: Implications for paleogeography, magmatism, and exhumation history of Iranian basement. Tectonophysics 451, 71–96.

Hawkesworth, C.J., Dhuime, B., Pietranik, A.B., Cawood, P.A., Kemp, A.I.S., Storey, C.D. 2010. The generation and evolution of the continental crust. J. Geol. Soc. 167 (2), 229-248.

Hellstrom, J., Paton, C., Woodhead, J., Hergt, J., 2008. Iolite: software for spatially resolved LA-(quad and MC) ICPMS analysis. In Sylvester, P. (Ed.), Laser Ablation ICP-MS in the Earth Sciences: Current Practices and Outstanding Issues. Mineral. Assoc. Can. Short Course 40, B. C., Vancouver, 343-348.

Horstwood, M.S.A., Košler, J., Gehrels, G., Jackson, S.E., McLean, N.M., Paton, C., … Schoene, B., 2016. Community-derived standards for LA-ICP-MS U–(Th–) Pb geochronology-uncertainty propagation, age interpretation and data reporting. Geostand. Geoanal. Res. 40, 311–332.

Jolivet, L., Faccenna, C., 2000. Mediterranean extension and the Africa – Eurasia collision. Tectonics 19, 1095 – 1106.

Khodabandeh, A.A., Aminifazl, A., 1993a. Geological map of 1/100000 Tasuj. Geological Survey of Iran.

Khodabandeh, A.A., Aminifazl, A., 1993b. Geological map of 1/100000 Salmas .Geological Survey of Iran.

Knipper, A., Ricou, L.E., Dercourt, J., 1986. Ophiolites as indicators of the geodynamic evolution of the Tethyan Ocean. Tectonophysics, 123, 213-240.

Le Bas, M.J., Le Maitre, R.W., Streekeisen, A., Zanettin, B., 1986. A chemical classification of volcanic rocks based on the total alkali-silica diagram. J. Petrol. 27, 745-750.

Leake, B.E., 1964. The Chemical Distinction Between Ortho- and Para-amphibolites, Dept. of Geology, The University of Bristol. J. Petrol. 5, 238-254.

Lechmann, A., Burg, J. P., Ulmer, P., Mohammadi, A., Guillong, M., Faridi, M., 2018. From Jurassic rifting to Cretaceous subduction in NW Iranian Azerbaijan: Geochronological and geochemical signals from granitoids. Contrib. Mineral.Petrol. 173 (12), 1-16.

Ludwig, K.R., 2003. User's Manual for Isoplot 3.00: A Geochronological Toolkit for Microsoft Excel. Berkeley Geochronology Center, Spec. Publ. 4.

McDonough, W.F., Sun, S.S., 1995. The composition of the Earth. Chem. Geol. 120, 223 – 253.

Mehdipour Ghazi, J., Moazzen, M., 2015. Geodynamic evolution of the Sanandaj-Sirjan Zone, Zagros Orogen, Iran. Turk. J. Earth Sci. 24, 513-528.

Misra, S.N., 1971. Chemical distinction of highgrade ortho- and para-metabasite. Nor. Geol. Tidsskr. 51, 311-316.

Mohajjel, M., Fergusson, C.L., 2000. Dextral transpression in Late Cretaceous continental collision, Sanandaj–Sirjan Zone, western Iran. J. Struct. Geol. 22, 125–1139.

Mohajjel, M., Fergusson, C.L., Sahandi, M.R., 2003. Cretaceous–Tertiary convergence and continental collision, Sanandaj–Sirjan zone, western Iran. J. Asian Earth Sci. 21, 397– 412.

Mohammadi, A., Burg, J.P., Guillong, M., 2022. The Siah Cheshmeh-Khoy-Misho-Tabriz fault (NW Iran) is a cryptic neotethys suture: evidence from detrital zircon geochronology, Hf isotopes, and provenance analysis. Int. Geol. Rev. 64 (2), 182-202.

Mohammadi, A., Moazzen, M., Lechmann, A., Laurent, O., 2020. Zircon U-Pb geochronology and geochemistry of Late Devonian–Carboniferous granitoids in NW Iran: implications for the opening of Paleo-Tethys. Int. Geol. Rev. 62 (15), 1931-1948.

Nabatian, G., Li, X.H., Honarmand, M., Esmaeili, R., 2021. The magmatic evolution of the Neotethyan rift: Geochronologic, isotopic, and geochemical evidence from A-type felsic magmatism, NW Iran. J. Geodyn. 145, 1-17.

O'Reilly, S. Y., Griffin, W. L., Pearson, N. J., Jackson, S. E., Belousova, E. A., Alard, O., Saeed, A.2008. Taking the pulse of the Earth: linking crustal and mantle events. Aust. J. Earth Sci. 55, 983-995.

Paton, C., Woodhead, J. D., Hellstrom, J. C., Hergt, J. M., Greig, A., Maas, R., 2010. Improved Laser Ablation U-Pb Zircon Geochronology through Robust Downhole FractionationCorrection. Geochem. Geophys. Geosyst. 11 (3), 1-36.

Pearce, J.A., Cann, J.R., 1973. Tectonic setting of basic volcanic rocks determined using trace element analysis. Earth Planet. Sci. Lett. 19 (2), 290-300.

Pearce, J.A., 1982. Trace element characteristics of lavas from destructive plate boundaries. In: Thorpe, R. S. (ed.) Andesites. Chichester: JohnWiley, 525-547.

Pearce, J.A., Stern, R.J. 2006. Origin of back-arc basin magmas: Trace element and isotope perspectives. Back-Arc Spreading Systems. Geol. Biol. Chem. Physic. 166, 63-86.

Pearce, T.H., Gorman, B.E., Birkett, T.C., 975. The TiO_2-K_2O-P_2O_5 diagram: A method of discriminating between oceanic and non-oceanic basalts. *Earth Planet.Sci. Lett.* 24, 419-426.

Petrus, J.A., Kamber, B.S., 2012. VizualAge: A Novel Approach to Laser Ablation ICPMS U-Pb Geochronology Data Reduction. Geostand. Geoanaly. Res. 36 (3), 247-270.

Pillevuit, A., Marcoux, J., Stampfli, G., Baud, A., 1997. The Oman exotics: a key to understanding of the Neotethyan geodynamic evolution. Geodinamica Act. 10 (5), 209– 238.

Saccani, E., Allahyari, Kh., Beccaluva, L., Bianchini, G., 2013. Geochemistry and petrology of the Kermanshah ophiolites (Iran): Implication for the interaction between passive rifting, oceanic accretion, and OIB-type components in the Southern Neo-Tethys Ocean. Gondwana Res. 24,392–411.

Schandl, E.S., Gorton, M.P. 2002. Application of high field strength elements to discriminate tectonic settings in VMS environments. Eco. Geol. 97, 629–642.

Scherer, E., Műnker, C., Mezger, K., 2001. Calibration of the Lutetium– Hafnium clock. Science, 293, 683–687. doi:10.1126/science. 1061372.

Searle, M.P., Graham, G.M., 1982. The "Oman Exotics": oceanic carbonate build-ups associated with the early stages of continental rifting. Geology 10, 43–9.

Shafaii Moghadam, H., Li, X.H., Griffin, W.L., Stern, R.J., Thomsen, T. B., Meinhold, G., … O'Reilly, S. Y., 2017. Early Paleozoic tectonic reconstruction of Iran: Tales from detrital zircon geochronology. *Lithos*, 268–271, 87–101.

Shafaii Moghadam, H., Griffin, W.L., Li, X.H., Santos, J.F., Karsli, O., Stern, R.J., … O'Reilly, S.Y., 2018. Crustal evolution of NW Iran: Cadomian arcs, Archean fragments and the Cenozoic magmatic flare-up. *J. Petrol.* 58 (11), 2143-2190.

Shafaii Moghadam, H., Li, Q. L., Li, X.H. Stern,R. J. Levresse, G., Santos, J. F., …Hassannezhad, A. 2020. Neotethyan Subduction Ignited the Iran arc and back-arc differently. *J. Geophys. Res.: Solid Earth*, 125 (5), 1-30.

Shafaii Moghaddam, H., Li, Q.L., Ling, X.X., Stern, R.J., Santos, J.F., Meinhold, G., … Shahabi, S. 2015. Petrogenesis and tectonic implications of Late Carboniferous A-type granites and gabbronorites in NW Iran: Geochronological and geochemical constraints. Lithos 212, 266-279.

Shahabpour, J., 2005. Tectonic evolution of the orogenic belt in the region located between Kerman and Neyriz. J. Asian Earth Sci. 24, 405–417.

Shakerardakani, F., Neubauer, F., Masoudi, F., Mehrabi, B., Liu, X., Dong, Y., … Friedl, G. 2015. Panafrican basement and Mesozoic gabbro in the Zagros orogenic belt in the Dorud–Azna region (nw Iran): Laser-ablation ICP–MS zircon ages and geochemistry. Tectonophysics, 647, 146–171.

549 Sláma, J., Košler, J., Condon, D.J., Crowley, J.L., Gerdes, M., Hanchar, J.M., …Whitehouse, M.J. 2008.
550 Plešovice zircon - A new natural reference material for U–Pb and Hf isotopic microanalysis. Chem. Geol.**,**
551 249 **(**1–2**)**, 1-35**.**
552
553 Stampfli, G.M., Hochard, C., Vérard, C., Wilhem, C., & von Raumer, J. 2013. The formation of Pangea.
554 Tectonophysics, 593, 1–19.
555
556 Stocklin, J., 1968. Structural history and tectonics of Iran: a review. *Am.Petrol. Geol. Bull.* 52, 1229-1258.
557
558 Sun, S.S., McDonough, W. F., 1989. Chemical and isotopic systematics of ocean basalts: Implications for
559 mantle composition and processes. In: Saunders, A. D., & Norry, M. J. (Eds.). Magmatism in the Ocean
560 Basins. *Geological Society of London, Special Publication,* 42, 313-345
561
562 Vertoort, J.D., Patchett, P.J., Blichert-Toft, J., Albarede, F., 1999. Relationships between Lu-Hf and Sm-
563 Nd isotopic systems in the global sedimentary system. *Earth and Planetary Science Letters,* 168, 79-99.
564
565 Vincent, S. J., Allen, M. B., Ismail-Zadeh, A. D., Flecker, R., Foland, K. A., & Simmons, M. D., 2005.
566 Insights from the Talysh of Azerbaijan into the Paleogene evolution of the South Caspian region.
567 *Geological Society of America Bulletin*, 117, 1513–1533.
568
569 Wiedenbeck, M., Alle, P., Corfu, F., Griffin, W. L., Meier, M., Oberli, F., … Spiegel, W., 1995. Three
570 natural zircon standards for U–Th–Ph, Lu–Th, trace element and REE analyses. Geostand. Newslett. 19
571 (1), 1–23.
572
573 Winchester, J.A., Floyd, P.A. 1977. Geochemical discrimination of different magma series and their
574 differentiation products using immobile elements. Chem. Geol. 20, 325-343.
575
576 Woodhead, J. D., Hergt, J.M. 2005. A preliminary appraisal of seven natural zircon reference materials
577 for *in situ* Hf isotope determination. Geostand. Geoanaly. Res. 29 (2), 183–195.
578
579 Zou, H.B., Zindler, A., Xu, X.S., Qu, Q. 2000. Major. Trace elements and Nd, Sr and Pb isotope studies of
580 Cenozoic basalts in SE China: mantle source, regional variations, and tectonic significance. *Chem. Geol.*
581 171, 33–47.
582

Figure caption

Fig. 1 Simplified geological map of Iran-Turkey showing the distribution of Cadomian basement rocks and Late Paleozoic rifting related rocks of Neotethys along the Bitlis-Zagros Zone (After Shafaii Moghadam et al., 2018 with some modifications). Further information represented in Table 1.

Fig. 2 Simplified geological map of the SE Salmas metamorphic complex (adopted from Tasuj and Salmas 1/100000 geological maps, Khodabandeh & Aminifazl, 1993a, b).

Fig. 3 Filed photographs of the SE Salmas metamorphic rocks. (a) Association of amphibolite, gneiss and recrystallized calcareous rocks, (b) outcropping of amphibolite at the west coast of Urmia Lake, (c) amphibolite enclave within gneiss, (d) fine- and medium-grained amphibolites more likely related to textural differences of basaltic and diabasic protolites.

Fig. 4 whole rock geochemical diagrams for the classification of SE Salmas amphibolites. (a) Zr/TiO_2 *vs* SiO_2 (Winchester & Floyd, 1977), (b) Ti/Y *vs* Nb/Y (Pearce, 1982), (c) Th *vs* Ta (Schandl & Gorton, 2002), (d) Ti/100-Zr-Y*3 (Pearce & Cann, 1973). Data for leucogabbro from the Salmas area are plotted for comparison. Symbols of star and pentagon show this study and Shafaii Moghadam et al., (2020), respectively.

Fig. 5 Nb *vs* Zr plots for SE Salmas amphibolites (Sun & McDonough, 1989).

Fig. 6 (a) Chondrite-normalized REE, (b) primitive mantle-normalised trace element diagrams for SE Salmas amphibolites. Normalized values are after McDonough & Sun, (1995).

Fig. 7 (a) U-Pb age *vs* εHf (t), (b) U-Pb age *vs* $^{176}Hf/^{177}Hf$ (t) for zircon from the SE Salmas amphibolites. Symbols are the same as FIGURE 4.

Fig. 8 (a) Zircon U-Pb concordia diagrams for the analysed zircons in SE Salmas amphibolites (sample SS20F), (b) Frequency histogram of the zircon $^{207}Pb/^{235}U$ ages from sample SS20B.

Fig. 9 (a-f) Summary of the Neotethys evolution and SE Salmas amphibolites formation. see text for explanations.

Table 1 Late Paleozoic within- plate extensional-related magmatic rocks from the Sanandaj-Sirjan Zone.

Area	Rock type	Magma type	Method	Age (Ma)	Tectonic setting	References
Nortth Sanandaj-Sirjan Zone (Iran)						
Heris	Granite	A-type	U-Pb	306±34	Within plate extensional	Advay and Ghalamghash, (2011)
Misho	Leucogabbro	-	U-Pb	356.7±3.4	Within plate extensional	Saccani et al., (2013)
Moro	Granite	A-type	U-Pb	351-356	Within plate extensional	Mohammadi et al., (2020)
Amand	Granite	A-type	U-Pb	350.9±1.3	Within plate extensional	Mohammadi et al., (2020)
Ajabshir	Rhyolite	A-type	U-Pb	332.5±2.2	Within plate extensional	Nabatian et al., (2021)
Qushchi	Amphibolite	-	U-Pb	274±75	Within plate extensional	This study
	Gabbronorite	-	U-Pb	316.8-319.9	Within plate extensional	Shafaii Moghadam et al., (2015)
	Gaggro-diorite	-	U-Pb	300-303	Within plate extensional	Asadpour et al., (2013b)
	Granite	A-type	U-Pb	317.3-322	Within plate extensional	Shafaii Moghadam et al., (2015)
	Alkaligranite-monzogranite	A-type	U-Pb	298-301	Within plate extensional	Asadpour et al., (2013b)
Ghazan	Gabbro	-	U-Pb	297±6	Within plate extensional	Asadpour et al., (2013a)
Khalifan	Granite	A-type	U-Pb	315±2	-	Bea et al., (2011)
Hassansalaran	Granite	A-type	U-Pb	360.7±5.6	Within plate extensional	Azizi et al., (2017)
Dorud-Azna	Mafic dyke	-	U-Pb	314.6±3.7	Within plate extensional	Shakerardakani et al., (2015)
Hassanrobat	Granite	A-type	U-Pb	288.3±3.6	Within plate extensional	Alirezaei and Hassanzadeh, (2012)
North Sanandaj-Sirjan Zone (Iraq)						
Damamna	Granite	A-type	U-Pb	364-372	Within plate extensional	Abdulzahra et al., (2016)
South Sanandaj Sirjan Zone (Iran)						
Sargaz-Abshour	Orthogneiss	-	U-Pb	317-322	Within plate extensional	Shafaii Moghadam et al., (2017)

Table 2 Whole rock XRF and ICP-MS analysis of amphibolites from the SE Salmas metamorphic complex.

Sample (%)	SS20F	SS26H	SS20B	SS20M	SS30D	Sample	SS20F	SS26H	SS20B	SS20M	SS30D
SiO_2	48.83	45.15	46.15	47.27	51.51	Gd (ppm)	5.86	11.18	3.93	4.4	15.05
TiO_2	2.23	2.62	1.95	1.83	1.23	Hf	4.9	6.7	3.1	3.2	21.4
Al_2O_3	14.55	16.62	16.24	16.15	17.72	Ho	1.04	1.86	0.87	1.0	2.68
Fe_2O_3*	11.83	15.29	13.25	12.65	12.15	La	19.8	43.6	11.1	12.3	73.9
MnO	0.18	0.21	0.2	0.19	0.21	Lu	0.33	0.65	0.37	0.38	0.9
MgO	6.27	4.44	6.68	6.36	1.25	Nb	22.3	39.9	12.5	13.6	45.1
CaO	9.21	7.5	8.36	8.13	5.19	Nd	24.8	48.8	13.7	15.7	73.5
Na_2O	2.84	3.32	3.07	3.17	4.8	Ni	78.3	43.3	75.4	73.1	3.3
K_2O	0.74	1.11	0.83	0.95	2.46	Pr	5.82	11.79	3.17	3.65	18.16
P_2O_5	0.35	0.91	0.19	0.23	0.59	Rb	17.2	27.7	31.2	37.6	48.1
BaO	0.02	0.04	0.03	0.03	0.08	Sc	27.1	22.9	28	26.7	15.2
Cr_2O_3	0.02	< 0.01	0.05	0.03	< 0.01	Sm	5.17	10.96	3.69	4.01	15.47
SrO	0.04	0.04	0.04	0.04	0.04	Sn	< 5	< 5	< 5	< 5	< 5
LOI	1.38	1.55	1.14	1.12	0.43	Sr	453	405.6	381.3	394.9	393
Total	98.7	98.7	99.07	98.25	98.19	Ta	1.6	2.7	0.8	1.0	1.7
Ba (ppm)	169.7	322.8	230.2	298.3	754.8	Tb	0.9	1.64	0.65	0.77	2.31
Ce	45.6	95.1	24.4	27.5	153.7	Th	6.24	4.31	3.09	1.68	5.09
Co	39.7	36.2	43.1	43.2	9.9	Tm	0.36	0.71	0.37	0.43	1.03
Cr	137	54	395	228	29	U	0.51	1.42	0.44	0.35	2.53
Cs	0.97	1.04	0.39	0.38	0.93	V	253	143	234	198	14
Dy	5.27	9.47	4.26	4.8	13.89	W	<1.0	< 1.0	< 1.0	1.0	<.01
Er	2.86	5.14	2.56	2.83	7.78	Y	26.6	47.8	22.9	25.9	73.7
Eu	1.82	3.14	1.37	1.43	4.29	Yb	2.4	4.25	2.35	2.63	5.94
Ga	20	25.7	17.8	18.3	35.7	Zr	172	292	119	118	844

Table 3 Zircon Hf data of amphibolites from the SE Salmas metamorphic complex.

Sample No.	Age (Ma)	$^{176}Lu/^{177}Hf$	2σ	$^{176}Hf/^{177}HF$	2σ	$(^{176}Hf/^{177}Hf)i$	εHf (t)	± 2s
SS20F-1	310	0.000811	0.000054	0.282778	0.000037	0.282773	6.5	1.0
SS20F-2	298.4	0.001256	0.000066	0.282807	0.000035	0.2828	7.2	1.0
SS20F-3	276	0.0004374	9.2E-06	0.282638	0.000052	0.282636	0.9	1.6
SS20F-4	297.8	0.0003	3.8E-06	0.282788	0.000026	0.282786	6.7	0.7
SS20F-5	296.2	0.001289	0.000064	0.282833	0.000036	0.282826	8.0	1.2
SS20F-6	294.9	0.000717	0.000064	0.282799	0.000028	0.282795	6.9	0.8
SS20F-7	296.8	0.00084	0.000015	0.282836	0.000035	0.282831	8.2	0.9
SS20F-8	298.4	0.001217	0.000062	0.282824	0.000035	0.282817	7.8	1.0
SS20F-9	303	0.000483	0.000063	0.282776	0.000032	0.282773	6.3	1.0
SS20F-10	313.5	0.0005999	0.000041	0.28279	0.000031	0.282786	7.0	1.0
SS20F-11	303.7	0.000956	0.000008	0.282808	0.000036	0.282803	7.4	1.0
SS20F-12	310.1	0.000487	0.000064	0.282783	0.000033	0.28278	6.7	0.8
SS20B-1	302.5	0.0005125	7.9E-06	0.282834	0.000064	0.282831	8.4	2.2
SS20B-2	99.1	0.00122	0.000068	0.282977	0.000045	0.282975	8.9	1.5
SS20B-3	105	0.001301	0.000028	0.282933	0.000044	0.28293	7.5	1.3
SS20B-4	104.8	0.001698	0.000078	0.283001	0.000042	0.282998	9.9	1.2
SS20B-5	99.5	0.001841	0.000062	0.283013	0.000041	0.28301	10.2	1.2
SS20B-6	307.7	0.0003408	2.4E-06	0.282961	0.000041	0.282959	13.0	1.2
SS20B-7	308.8	0.0004185	0.000005	0.282998	0.00031	0.282996	14.3	1.0
SS20B-8	108.5	0.00241	0.00013	0.283034	0.000043	0.282998	11.0	1.3
SS20B-9	65.4	0.000802	0.000047	0.282838	0.000037	0.282837	3.3	1.0
SS20B-11	301	0.00046	0.000016	0.282984	0.000042	0.282981	13.7	1.2

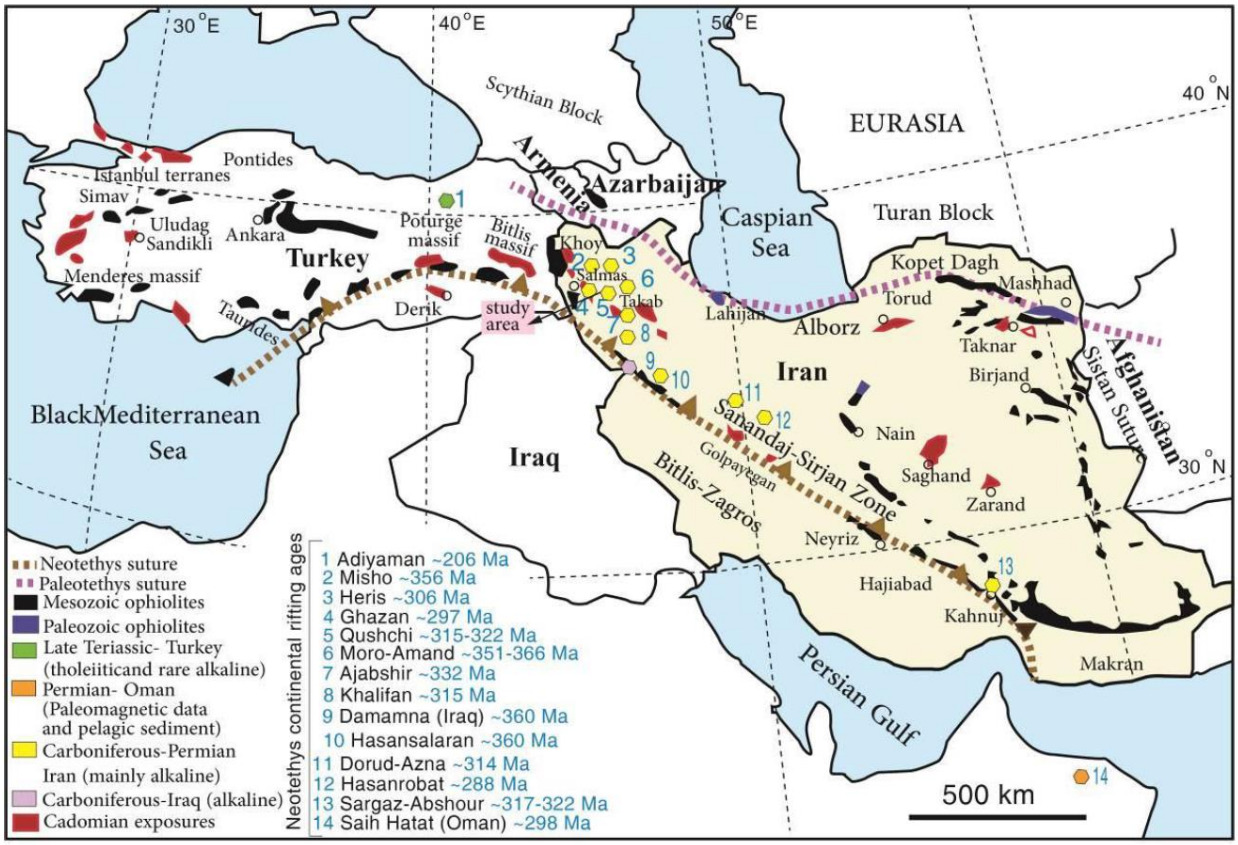
30°E
40°E
50°E
40°N
30°N
Scythian Block
EURASIA
Armenia
Azarbaijan
Caspian Sea
Turan Block
Pontides
Istanbul terranes
Simav
Uludag
Sandikli
Ankara
Turkey
Menderes massif
Taurides
Poturge massif
Bitlis massif
Derik
study area
Khoy
Salmas
Takab
Lahijan
Alborz
Kopet Dagh
Mashhad
Torud
Taknar
Birjand
Iran
Afghanistan
Sistan Suture
Black Sea
Mediterranean Sea
Iraq
Sanandaj-Sirjan Zone
Golpayegan
Bitlis-Zagros
Nain
Saghand
Zarand
Neyriz
Hajiabad
Kahnuj
Makran
Persian Gulf
500 km
Neotethys suture
Paleotethys suture
Mesozoic ophiolites
Paleozoic ophiolites
Late Teriassic- Turkey (tholeiiticand rare alkaline)
Permian- Oman (Paleomagnetic data and pelagic sediment)
Carboniferous-Permian Iran (mainly alkaline)
Carboniferous-Iraq (alkaline)
Cadomian exposures
Neotethys continental rifting ages
1 Adiyaman ~206 Ma
2 Misho ~356 Ma
3 Heris ~306 Ma
4 Ghazan ~297 Ma
5 Qushchi ~315-322 Ma
6 Moro-Amand ~351-366 Ma
7 Ajabshir ~332 Ma
8 Khalifan ~315 Ma
9 Damamna (Iraq) ~360 Ma
10 Hasansalaran ~360 Ma
11 Dorud-Azna ~314 Ma
12 Hasanrobat ~288 Ma
13 Sargaz-Abshour ~317-322 Ma
14 Saih Hatat (Oman) ~298 Ma

Fig. 1

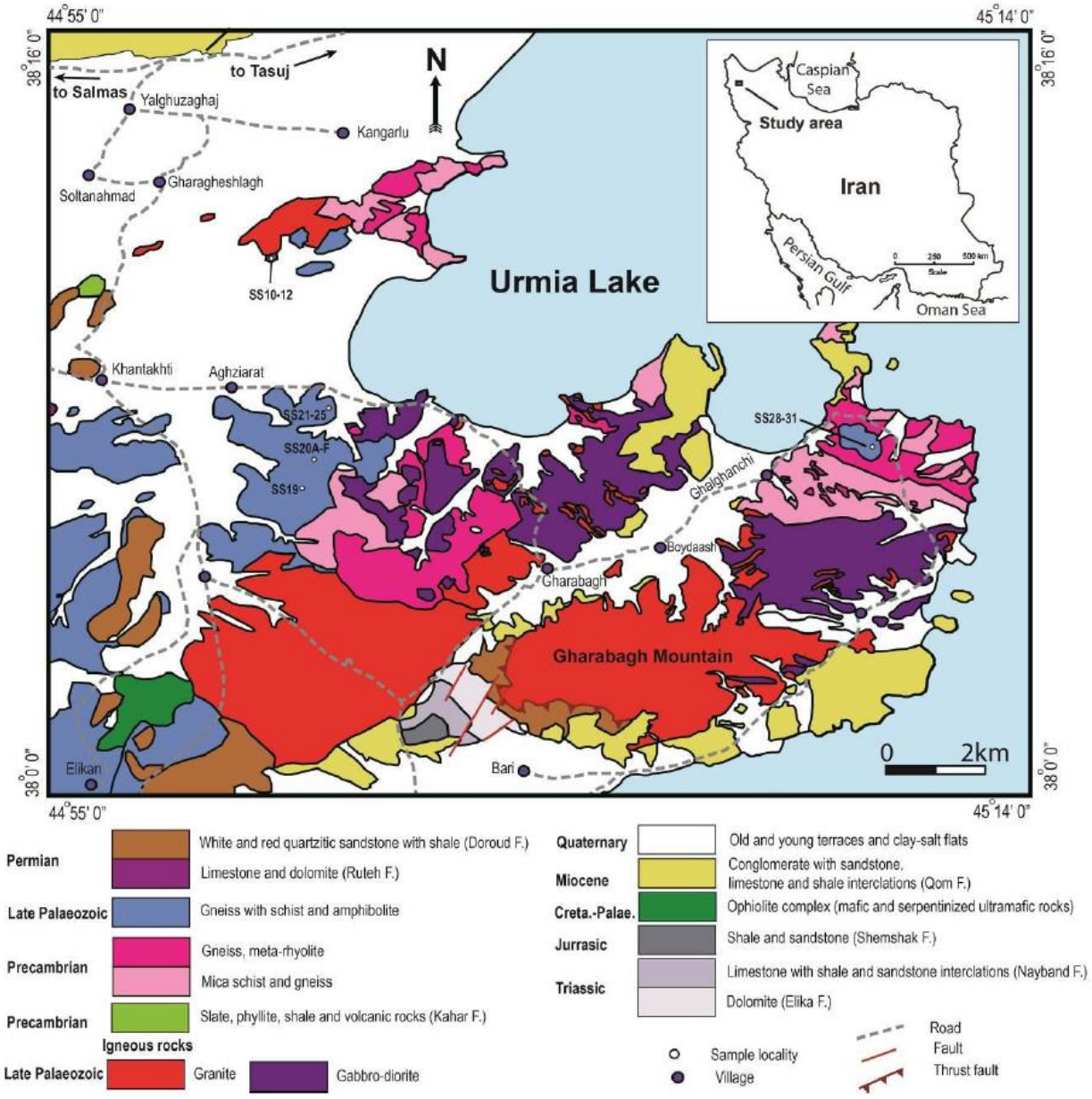
44°55' 0"
45°14' 0"
38°16' 0"
38°0' 0"
N
to Tasuj
to Salmas
Yalghuzaghaj
Kangarlu
Soltanahmad
Gharagheshlagh
SS10-12
Urmia Lake
Caspian Sea
Study area
Iran
Persian Gulf
Oman Sea
Khantakhti
Aghziarat
SS21-25
SS20A-F
SS19
SS28-31
Ghalghanchi
Boydaash
Gharabagh
Gharabagh Mountain
Elikan
Bari
0 2km
Permian
White and red quartzitic sandstone with shale (Doroud F.)
Limestone and dolomite (Ruteh F.)
Late Palaeozoic
Gneiss with schist and amphibolite
Precambrian
Gneiss, meta-rhyolite
Mica schist and gneiss
Precambrian
Slate, phyllite, shale and volcanic rocks (Kahar F.)
Igneous rocks
Late Palaeozoic
Granite
Gabbro-diorite
Quaternary
Old and young terraces and clay-salt flats
Miocene
Conglomerate with sandstone, limestone and shale interclations (Qom F.)
Creta.-Palae.
Ophiolite complex (mafic and serpentinized ultramafic rocks)
Jurrasic
Shale and sandstone (Shemshak F.)
Triassic
Limestone with shale and sandstone interclations (Nayband F.)
Dolomite (Elika F.)
Sample locality
Village
Road
Fault
Thrust fault

Fig. 2


(a)
Gneiss
Amphibolite
Marble
S
N
(b)
Urmia Lake
Marble
Amphibolite
S
N
(c)
Amphibolite
Gneiss
(d)
Fine-grained
amphibolite
Medium-grained
amphibolite

Fig. 3

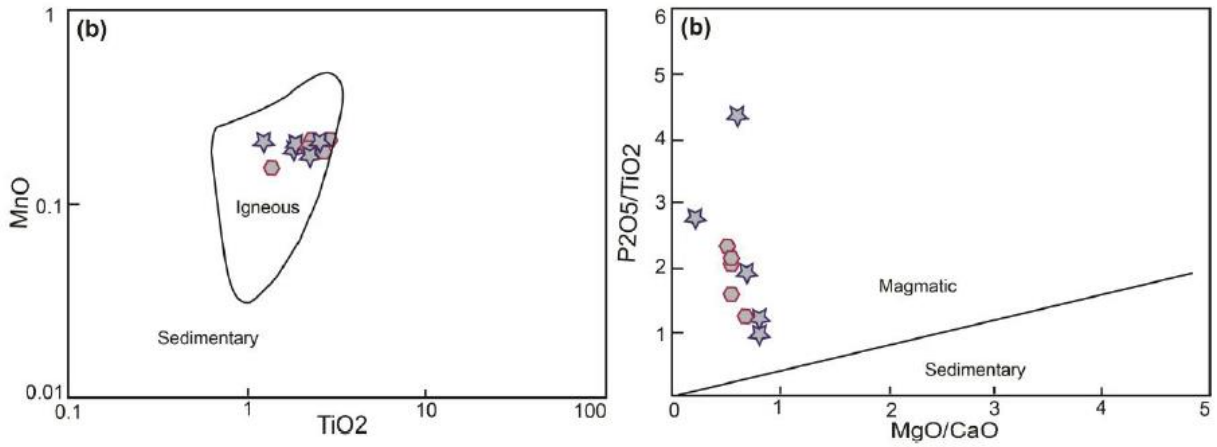
(b)
MnO
TiO2
Igneous
Sedimentary
0.01
0.1
1
10
100
(b)
P2O5/TiO2
MgO/CaO
Magmatic
Sedimentary
0
1
2
3
4
5
6

Fig. 4

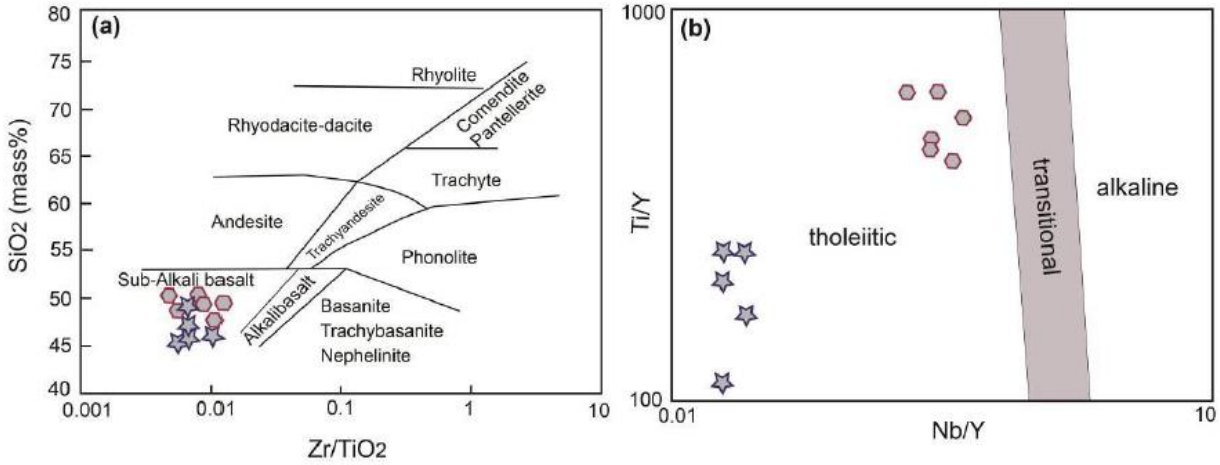
(a)
Rhyolite
Comendite
Pantellerite
Rhyodacite-dacite
Trachyte
Andesite
Trachyandesite
Phonolite
Sub-Alkali basalt
Alkalibasalt
Basanite
Trachybasanite
Nephelinite
SiO2 (mass%)
Zr/TiO2
(b)
tholeiitic
transitional
alkaline
Ti/Y
Nb/Y

Fig. 5

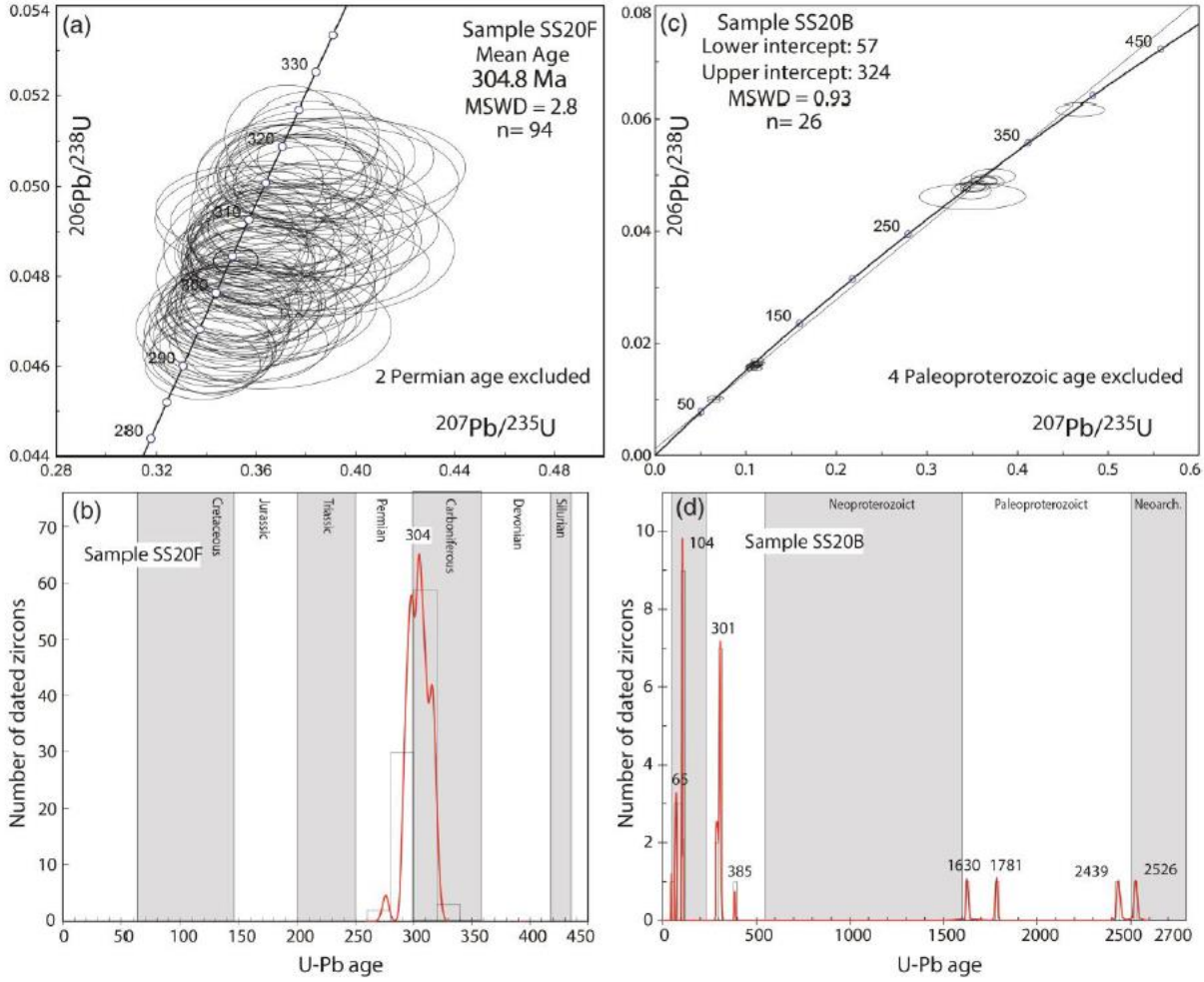
(a)
Sample SS20F
Mean Age
304.8 Ma
MSWD = 2.8
n= 94
2 Permian age excluded
206Pb/238U
207Pb/235U
(c)
Sample SS20B
Lower intercept: 57
Upper intercept: 324
MSWD = 0.93
n= 26
4 Paleoproterozoic age excluded
(b)
Sample SS20F
Cretaceous
Jurassic
Triassic
Permian
Carboniferous
Devonian
Silurian
Number of dated zircons
U-Pb age
(d)
Sample SS20B
Neoproterozoict
Paleoproterozoict
Neoarch.
U-Pb age

Fig. 6

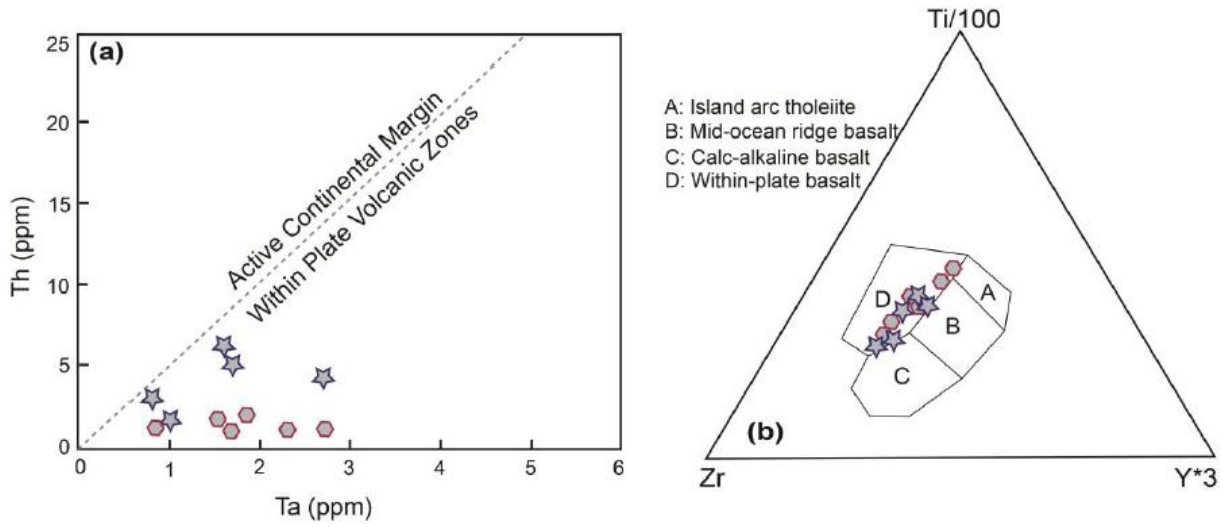
(a)
Active Continental Margin
Within Plate Volcanic Zones
Th (ppm)
Ta (ppm)
0
5
10
15
20
25
0
1
2
3
4
5
6
Ti/100
A: Island arc tholeiite
B: Mid-ocean ridge basalt
C: Calc-alkaline basalt
D: Within-plate basalt
A
B
C
D
(b)
Zr
Y*3

Fig. 7

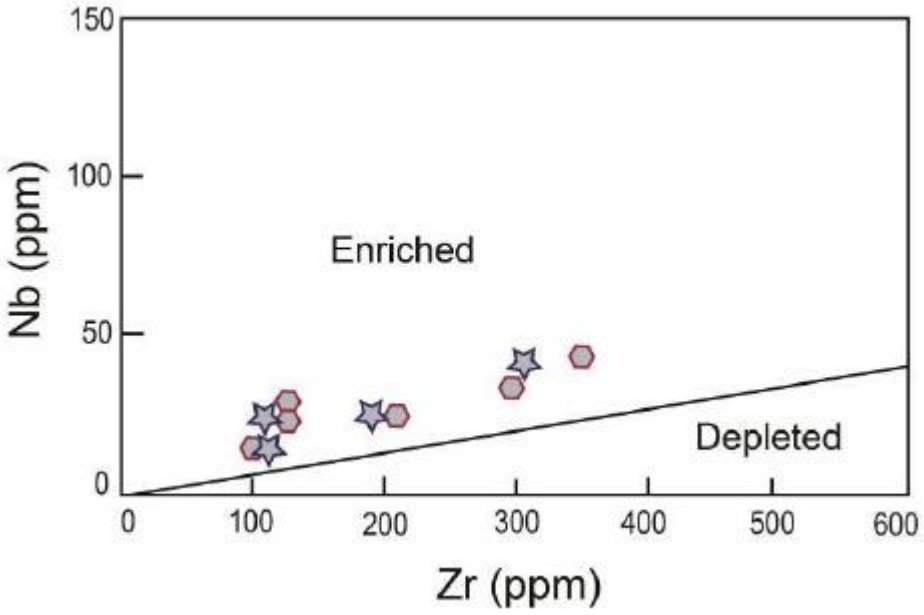
Nb (ppm)
Zr (ppm)
Enriched
Depleted
0
50
100
150
0
100
200
300
400
500
600

Fig. 8

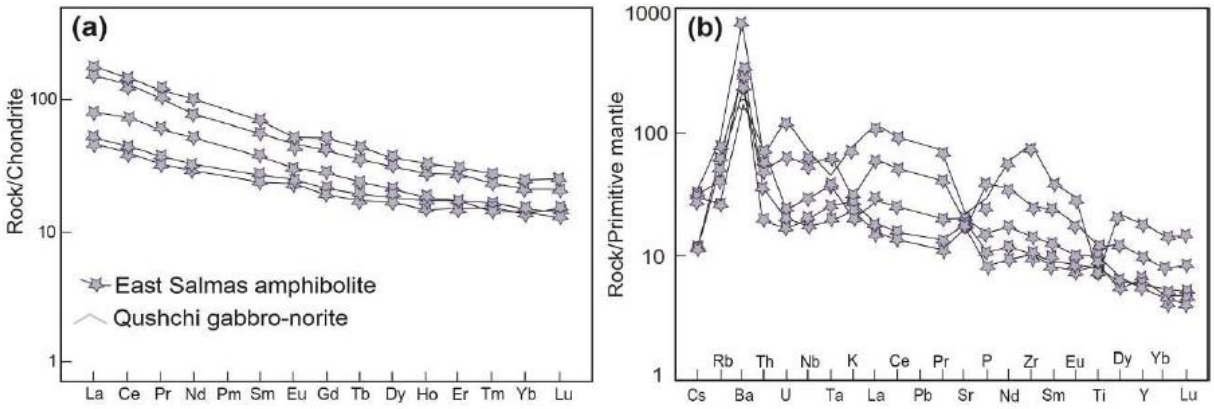
(a)
Rock/Chondrite
100
10
1
East Salmas amphibolite
Qushchi gabbro-norite
La Ce Pr Nd Pm Sm Eu Gd Tb Dy Ho Er Tm Yb Lu
(b)
Rock/Primitive mantle
1000
100
10
1
Cs Rb Ba Th U Nb Ta K La Ce Pb Pr Sr P Nd Zr Sm Eu Ti Dy Y Yb Lu

Fig. 9

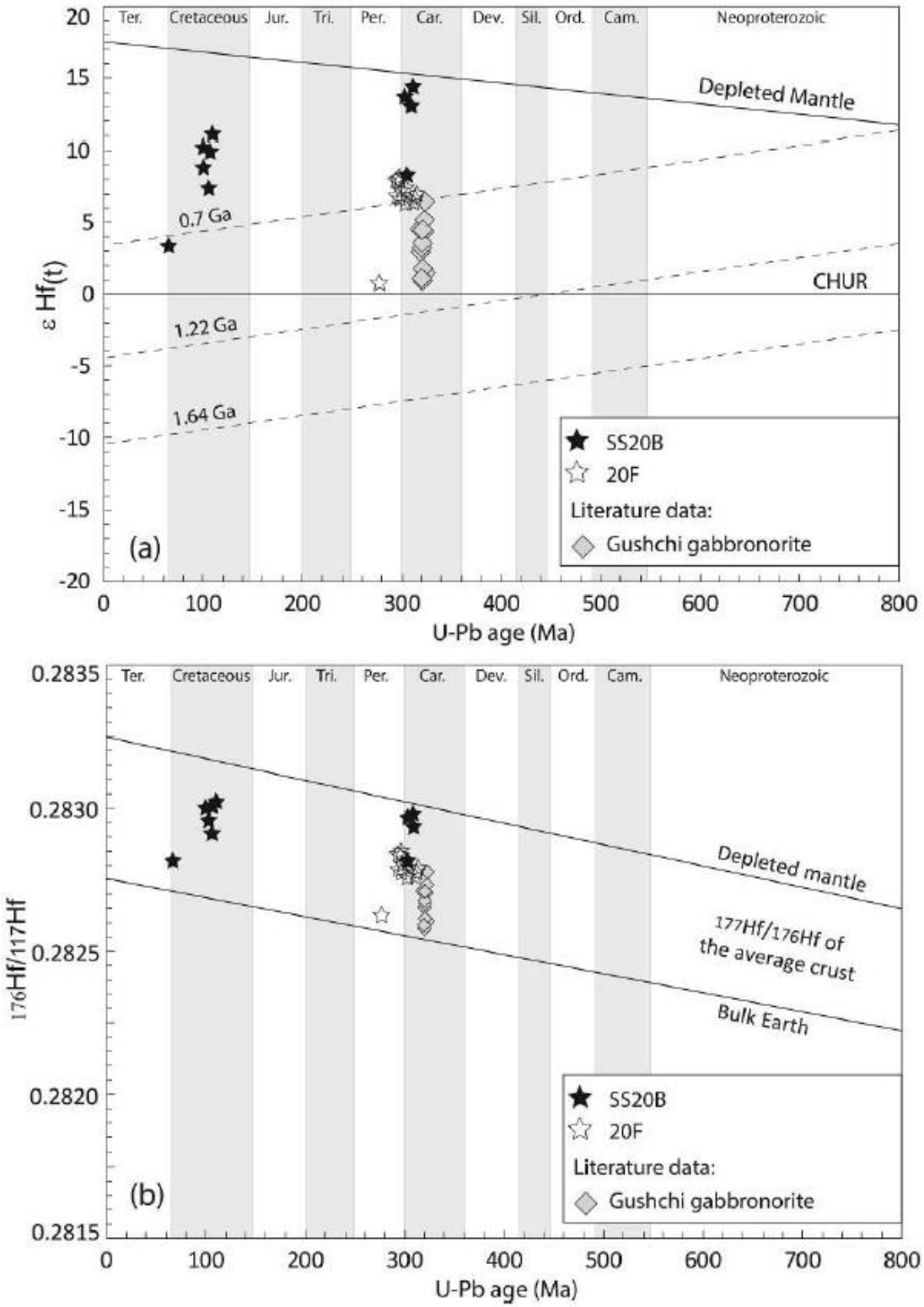
Ter.
Cretaceous
Jur.
Tri.
Per.
Car.
Dev.
Sil.
Ord.
Cam.
Neoproterozoic
Depleted Mantle
CHUR
0.7 Ga
1.22 Ga
1.64 Ga
ε Hf(t)
U-Pb age (Ma)
SS20B
20F
Literature data:
Gushchi gabbronorite
(a)
(b)
Depleted mantle
177Hf/176Hf of the average crust
Bulk Earth
176Hf/117Hf

Fig. 10

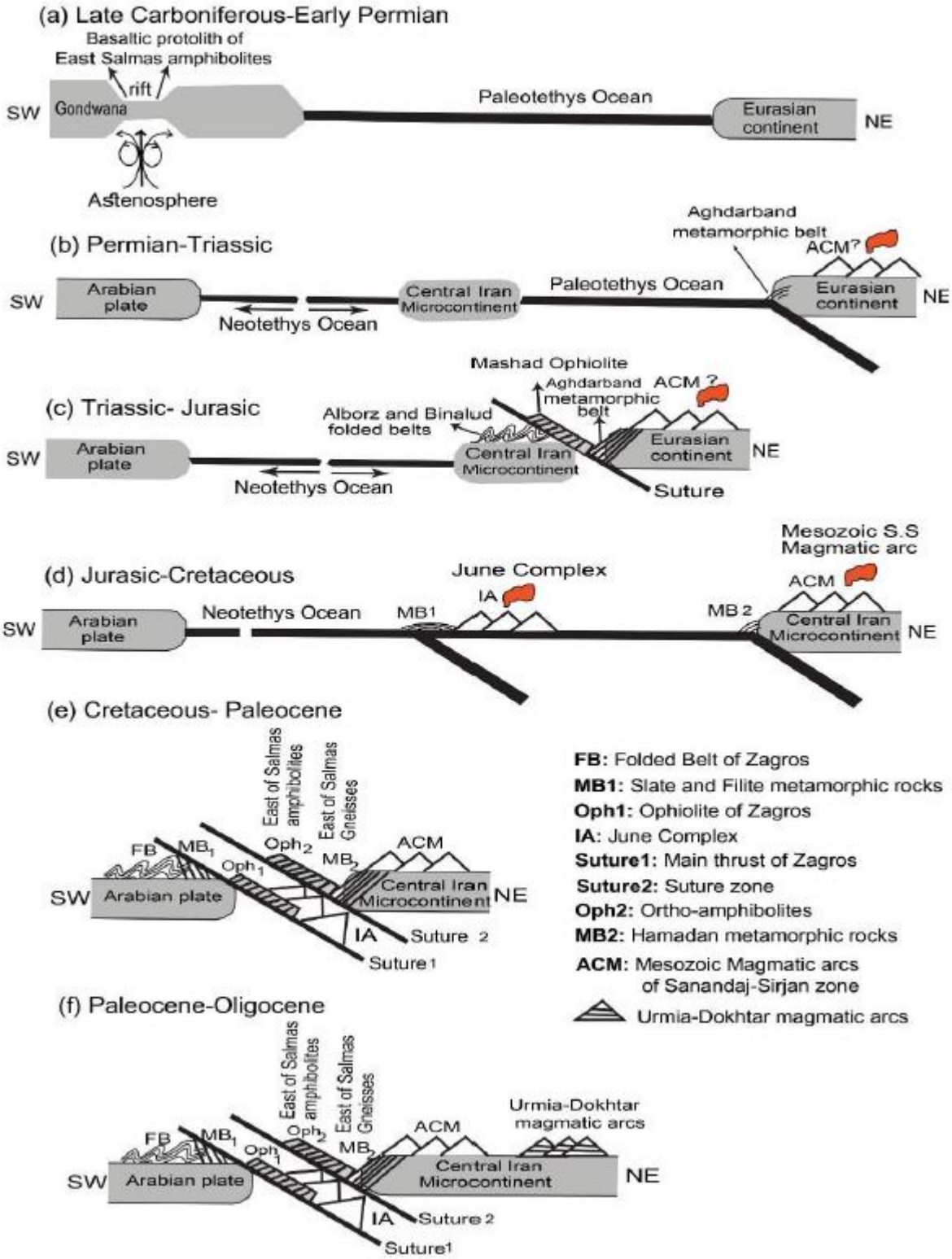
(a) Late Carboniferous-Early Permian
Basaltic protolith of
East Salmas amphibolites
rift
SW
Gondwana
Paleotethys Ocean
Eurasian continent
NE
Astenosphere
(b) Permian-Triassic
Aghdarband metamorphic belt
ACM?
SW
Arabian plate
Central Iran Microcontinent
Paleotethys Ocean
Eurasian continent
NE
Neotethys Ocean
(c) Triassic- Jurasic
Mashad Ophiolite
Aghdarband metamorphic belt
ACM ?
Alborz and Binalud folded belts
SW
Arabian plate
Central Iran Microcontinent
Eurasian continent
NE
Neotethys Ocean
Suture
(d) Jurasic-Cretaceous
Mesozoic S.S Magmatic arc
June Complex
ACM
IA
SW
Arabian plate
Neotethys Ocean
MB1
MB 2
Central Iran Microcontinent
NE
(e) Cretaceous- Paleocene
East of Salmas amphibolites
East of Salmas Gneisses
FB
MB1
Oph2
Oph1
MB2
ACM
SW
Arabian plate
Central Iran Microcontinent
NE
IA
Suture 2
Suture1
FB: Folded Belt of Zagros
MB1: Slate and Filite metamorphic rocks
Oph1: Ophiolite of Zagros
IA: June Complex
Suture1: Main thrust of Zagros
Suture2: Suture zone
Oph2: Ortho-amphibolites
MB2: Hamadan metamorphic rocks
ACM: Mesozoic Magmatic arcs of Sanandaj-Sirjan zone
Urmia-Dokhtar magmatic arcs
(f) Paleocene-Oligocene
East of Salmas amphibolites
East of Salmas Gneisses
Urmia-Dokhtar magmatic arcs
FB
MB1
Oph2
Oph1
MB2
ACM
SW
Arabian plate
Central Iran Microcontinent
NE
IA
Suture 2
Suture1

Fig. 11